Effects of Defect Density on the FIR Radiation Spectra of Anatase TiO_2 Powder

Seunghee Lee[a, b], Shinhoo Kang[a, b, *]

[a] Program in Physics, Graduate School of Science, Royal University of Phnom Penh, Phnom Penh 120101-121208, Cambodia
[b] Department of Materials Science and Engineering, College of Engineering, Seoul National University, Seoul 151-742, Korea

***Corresponding Author:** shinkang@snu.ac.kr
https://doi.org/10.55674/jmsae.v14i1.257905

Received: 13 August 2024 | **Revised:** 22 October 2024 | **Accepted:** 24 October 2024 | **Available online:** 01 January 2025

Abstract

Anatase TiO_2 powder shows an excellent emissivity of 0.916 over the wavelength range of 7 ~ 20 μm at 250°C; however, it shows a relatively low emissivity of 0.767 over the range of 3 ~ 7 μm. We investigated the effect of structural defects on the radiation properties of anatase TiO_2 powder by introducing point and line defects into the system. The emissivity over the range of 3 ~ 7 μm increased from 0.767 – 0.902 upon the introduction of appropriate quantities of oxygen vacancies. This result suggested that the radiation properties are related in part to electronic transitions and could be significantly improved by optimizing the crystallinity of the host material. The results from X-ray diffraction (XRD), Fourier-transform infrared spectrometer (FT-IR), and Raman spectroscopy were used to explain the observations, along with predictions by a discrete variational X-α (DV-Xα) molecular orbital simulation.

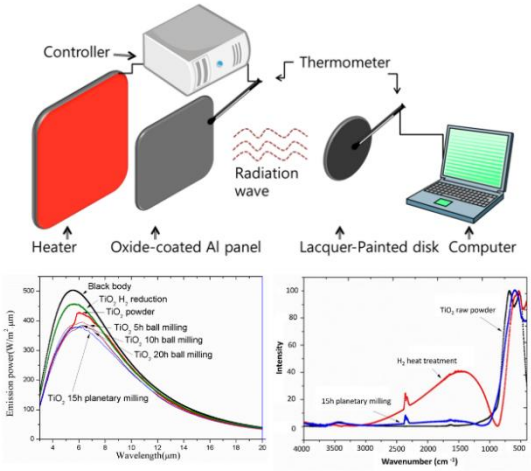

Keywords: Far-infrared radiation; Energy level; DV-Xα; TiO_2; Electron states.

Introduction

Far infrared (FIR) radiation is widely used for heating purposes in our daily lives because its energy corresponds to the absorption wavelength of various organic compounds [1, 2]. The benefits of far-infrared drying include homogeneous heating, low energy usage, quick drying times, and less material degradation as a result. In the drying process, a single far-infrared radiation source significantly improves heat transmission but has no influence on mass transfer. Because ultrasonic strengthening encourages mass transfer of materials, far-infrared radiation and ultrasonic radiation may be used to improve mass transfer of materials and heat at the same time. This will increase the pace of dehydration and improve the quality of the final product. Agricultural items such as kiwifruit [3], pumpkin [4], jackfruit [5], and banana [6] have been effectively dried using direct-touch ultrasonic far-infrared technology in recent times. The intensity of radiation emitted from a heated material is proportional to T^4, regardless of the nature of the material, as described by Kirchhoff's law. The emissivity and energy emitted are commonly measured with respect to the properties of an ideal object, a black body [7]. Natural inorganic materials are classified as high-efficiency radiators, FIR radiators, or low-efficiency radiators, depending on the temperature-dependent intensity of the FIR emission spectrum. To increase the radiation efficiency, such materials may be mixed in varying ratios, or transition elements may be added to them. However, few studies have examined the FIR radiation characteristics of a material as a function of the crystal structure or in terms of its molecular, atomic, or electronic energy structure [8, 9]. Metal oxides including SiO_2, Al_2O_3, and TiO_2 are commonly found in FIR emitting ceramics [10 – 12]. Numerous-component natural minerals, including tourmaline, kaolinite, and rhyolite, have been investigated for their special qualities [12 – 21]. As previously indicated, these FIR-emitting minerals and ceramics have potential for use in functional fabrics and clothing with a range of health advantages, as well as for heat management applications [22]. Inorganic minerals have

also shown to have other advantages, such as antibacterial qualities. Athletes using socks with FIR emitting minerals have exhibited less perspiration and bacterial development in prior research [23]. When compared to surface coating techniques for finishing treatment, the integration of mineral particles into polymers to form polymer composites often carries the least amount of risk [24]. Because of their minuscule particle size at the nanoscale, there have been recent worries about the use of nanoparticles and their possible effects on the skin of wearers [25]. In order to assure the safe and responsible use of nanoparticles and reduce any negative effects, further research is required to examine the effects of nanoparticles on the skin and environment. TiO_2 is a typical material for FIR applications. The ability of inorganic oxides to screen ultraviolet light (UV) has been found [26]. In particular, the Food and Drug Administration (FDA) of the United States has authorized zinc oxide (ZnO) and titanium dioxide (TiO_2) for use in sunscreens [27]. By measuring the transmission and reflection characteristics of micron and nano ZnO and TiO_2 particles using optical sampling equipment, Cole et al. showed that the main source of these inorganic UV filters' UV protection effects is their absorption capacity rather than their scattering and reflecting abilities [28]. The band gap width of TiO_2 and ZnO particles, which are semiconducting materials, determines how efficiently they scatter and reflect visible light as well as absorb UV radiation. UV absorption occurs when the energy absorption exceeds the band gap width, as elucidatpr in previous studies on the band gap theory [29 – 31]. Iron oxides, including hematite, have demonstrated the ability to absorb ultraviolet light recently. Hoang-Minh et al. created a variety of clays and discovered that a clay's capacity to block UV light is significantly influenced by its Fe_2O_3 level. Similar to TiO_2, the primary cause may be linked to the empty orbital in $Fe3^+$ electron structure and energy absorption in the near UV, which results in a shift to a higher energy level [32]. In addition to offering limited protection against near-infrared radiation and high-energy visual (HEV) light, TiO_2 and ZnO are primarily responsible for UVA and UVB protection. Iron oxide has proven to be an efficient shield against HEV radiation, which is primarily responsible for the photoaging of skin and has a wavelength between 400 and 500 nm [33]. These days, there are more people worrying about the safety of TiO_2 and ZnO particles due to their potential to produce reactive oxygen species (ROS) when exposed to UV radiation due to their photocatalytic properties. Because the surface characteristics of these particles affect the photocatalytic effects, coatings containing other materials, including silica, are used as a safeguard against possible problems [34]. The photocatalytic activity of ZnO can be decreased by adding metal atoms like Al, Mn, and Na because they can cause deep bandgap impurity levels and function as recombination traps for excitons produced by photosynthesis [35]. It was also shown that iron oxide has a very small photocatalytic impact when compared to TiO_2 and ZnO [36]. Therefore, natural mineral powder containing iron oxide, as well as a combination of metal atoms with photocatalytic oxides such as TiO_2 and ZnO, may also possess potential UV protection ability. In our previous study [37], based on a discrete variational X-α (DV-Xα) simulation, the effectiveness of FIR radiation of various Ti-based oxides was related in part to the electron transition. The experiment revealed that Ti_2O_3 and TiO_2 were more effective FIR source materials than TiO_2, and the presence of a band gap in TiO_2 was considered, to some extent, to be the cause of the relatively low FIR emission intensity. In this study, planetary ball milling and hydrogen reduction heat treatment were applied to TiO_2 anatase powder to modify the emissivity over a wavelength range of 3 ~ 7 μm. DV-Xα computer simulations were also used to calculate the electronic energy levels of the material [38 – 41]. The intensity of radiation from each energy level was estimated using the simulation results, and was compared with the experimental results to understand the contribution of electron transitions to the FIR radiation.

Materials and Methods

TiO_2 powder (99+% purity, anatase, <110 μm, Aldrich) was used in the experiment. The powder was milled via ball milling or planetary milling for various defect densities (herein referred to as as-milled powder). For the ball milling process (intermediate defect density), WC-Co balls and TiO_2powder were mixed and milled in a plastic jar. The ball-to-powder weight ratio was 10:1, and milling was performed under dry condition at 220 rpm for 5, 10, and 20 h. On the other hands, for the planetary milling process (high defect density), WC-Co balls and a WC-Co-coated jar were employed. The ball-to-powder weight ratio was 30:1, and milling was performed under dry conditions at 250 rpm for 15 or 30 h. All milled powder was screened with a 325-mesh sieve for the experiments. To investigate the effects of low defect density, the as-received samples were reduced at 1,200°C for 3 h in an alumina tube furnace with a heating and cooling rate of 10° C min^{-1}. A mixed gas containing 5% hydrogen and 95% nitrogen was used for reduction at a flow rate of 200 sccm. Two grams of each sample were mixed with a binder in a ratio of 1:1 in weight. The binder consisted

of water-glass (a sodium silicate solution, Na_2SiO_3) and water, which were mixed in a ratio of 1:10. The solution was then coated onto an aluminum panel (200 × 200 × 0.50 mm^3). Fig. 1 shows a schematic diagram of the devices used to measure the heating effects of FIR radiation. Coated aluminum panels were used as FIR sources by maintaining the panels at 250°C. Another aluminum disk (diameter: 200 mm; thickness: 0.50 mm) was painted with a nitrocellulose lacquer (Samwha, Korea) to a thickness of 20 μm and was positioned at 30, 60, or 90 cm away from the FIR source panel. The temperature increase of the paint was measured using a thermometer (Thermometer-1316 TES, Taiwan). The emissivity and radiation energy of the sample material were measured using a Fourier-transform infrared (FT-IR) spectrometer (Midac 2200, USA) at a fixed temperature of 250°C. The measurements were conducted over the range 4,000 ~ 400 cm^{-1}, and the resolution of the equipment was 8 cm^{-1}. A Raman spectrometer (Horiba T64000, France) and a high-temperature FT-IR spectrophotometer (Thermo Scientific 6700, USA) were used to analyze the structure and characteristics of the samples. A TC400 Nitrogen/oxygen analyzer (Leco, USA) was used to analyze the oxygen content in the samples. XRD analysis was performed to analyze the phases after H_2reduction or planetary milling. The FIR energy spectrum radiated from the TiO_2 system was estimated by modeling a crystalline cluster of TiO_2 (anatase) using the DV-Xα program to calculate the energy levels [42 – 44].

Results and Discussions

Radiation Properties of the Various TiO_2 Phases

Previously nitrocellulose lacquer paint showed good resonance and absorption spectra when Ti-based oxide systems were used as FIR sources at 250°C [37]. Thus, the temperature sensitivity of the measurement setup was checked over the range 5 ~ 20 μm at 40°C. The results showed that the measured radiation energy was constant, ~360 W m^{-2}, across the whole range and that the emissivity was 0.890 ± 0.025. The temperature increases of the aluminum disk coated with paint were also measured as a function of the radiated energy. The mean values of the temperature increase of the TiO_2 raw sample were 12.58°C, 4.25°C, and 1.88°C at distances of 30, 60, and 90 cm, respectively.

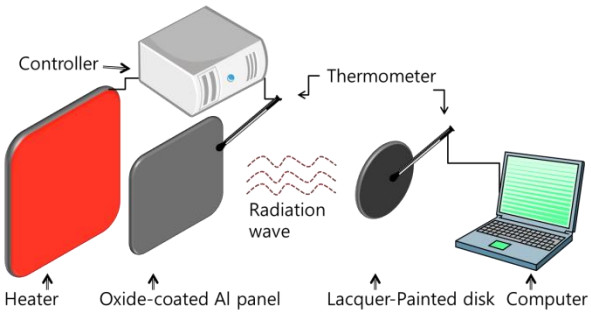

Fig. 1 Schematic view of the experimental system.

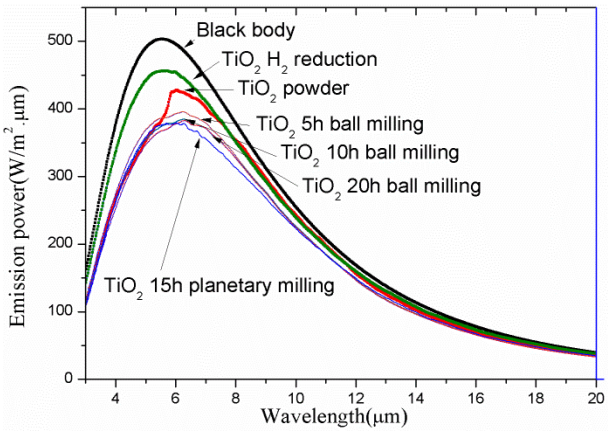

Fig. 2 Emissive power of various TiO_2 samples with respect to a blackbody (250°C, 3 ~ 20 μm).

The mean of the five measurements, with a standard deviation of less than ± 1.20°C, demonstrated that the FIR measuring apparatus yielded reproducible measurements of FIR radiation power. Table 1 shows the measured radiation energy changes for each sample. All data were collected after 90 s as a function of the distance and of the powder conditions. The aluminum panel without a coating showed the lowest temperature increase of 3.03°C at a 30 cm distance, whereas the panel coated with the water-glass binder showed a temperature increase of 4.25°C at this distance. When 2 g of a TiO_2 powder was used together with the water-glass binder, significant differences were observed. At the same distance, the milled TiO_2 powder showed an increase of 17.70°C, and the reduced powder showed a higher increase of 24.38°C. The influence of the binder, therefore, was small, and the difference resulted from the presence of the TiO_2 powder in the coating. However, the TiO_2 raw sample showed a relatively low increase of

Table 1 Temperature increases in the aluminum disks coated with lacquer paint under FIR irradiation from the various TiO_2-coated disks. ΔT: Temperature increase with respect to room temperature.

Distance (cm) / FIR coating	ΔT (°C)		
	30	**60**	**90**
No coating	3.03±0.65	0.58±0.51	0
Water-glass binder	4.25 ±0.60	0.75±0.50	0
TiO_2 raw powder	12.58±0.35	4.25±0.20	1.88±0.94
15 h milling	17.70±1.20	4.35±0.45	2.02±0.25
H_2 reduction	24.38±1.10	5.58±0.25	2.55±0.75

Table 2 Emissivity of the various TiO_2 samples at 250°C, measured from the FT-IR spectra.

Wavelength	**3~7 (μm)**	**7~11 (μm)**	**11~15 (μm)**	**15~20 (μm)**	**Average**
Black body	1	1	1	1	1
Powder	0.767	0.943	0.918	0.886	0.878
15 h milling	0.731	0.851	0.877	0.871	0.833
H_2 reduction	0.902	0.935	0.945	0.946	0.932

12.58°C, and the increases at distances of 60 and 90 cm showed the same tendency. The radiation of FIR energy, which was comparable to the molecular vibrational energies in the paint dyes, increased the temperature of the aluminum disk due to the generation of heat via molecular stretching and rotational modes due to the resonance effect [45]. The results demonstrate that the intensity of FIR radiation from a material depends on the amounts of defects caused in the system by treatment method, such as the milling or reduction, even though the materials are all essentially composed of TiO_2. The milling process may introduce significant disorder into the crystalline structure, even producing an amorphous state. Various defects can alter the electron energy levels and, consequently, the radiation properties of the TiO_2 sample. The XRD results discussed in the following section demonstrate the level of disorder by milling. Reduction in a N_2–H_2 atmosphere produces mostly point defects in nature; i.e., oxygen vacancies in the TiO_2. The presence of point defects also causes distortions of crystalline structure. Optimizing the level of disorder would improve the FIR radiation spectrum. The results shown in Table 1 indicate that the low concentration of point defects produced by the reduction process resulted in notably enhanced FIR properties. Fig. 2 shows the distributions of the emission power of various TiO_2 samples measured by FT-IR spectrometry at 250°C. Of all samples the reduced sample in N_2-H_2 gas demonstrated the highest emission intensity. Also, it yielded an asymmetric spectrum shape which is similar to that of black body. Its peak wavelength is found consistent with Wien's law, 5.54 μm. However, the emission power of the anatase TiO_2 sample is low and the curve deviates from the curve shape of the other materials, especially over the 3 ~ 7 μm range as discussed in our previous work [37]. On the other hand, all milled samples result insignificant decreases in emissivity, and the emissivity is even lower than that of raw anatase TiO_2. The milling time and intensity do not appear to cause much difference in the emissivity, which is in contrast to our expectation. For example, the planetary-milled powder intended for high structural disorder shows almost the same emission power as that of the powder ball-milled for a low defect density. All milled samples also show peak shifts toward 6.50 μm, and the spectra shape becomes more symmetric compared to that of a black body. Table 2 summarizes the relative emissivity of various TiO_2 samples relative to that of a black body. Of the various samples, the reduced sample showed the highest emissivity, 0.902 ~ 0.946 μm, over all ranges. The TiO_2 raw sample had a mean emissivity of 0.878, even if it had an especially low value of 0.767 over the 3 ~ 7μm range. The spectra of the powder planetary-milled for 15 h show a gradual rise from 0.731 over the range 3 ~ 11 μm. The level of disorder in the planetary-milled sample was expected to be higher than the ball-milled sample. The difference in emissivity between the two milled powder samples was a mere 0.023. It implies that there exists a low threshold in defect intensity for the

enhancement of emission property, <5 h ball milling. line and planar defects obtained from milling process could be detrimental to emission property. The observed trend was the same as that observed in the temperature measurements listed in Table 1. A close relationship between the defect density and emissivity is likely, and this relationship maybe controlled only when the defect density is low.

Structural analysis

Fig. 3 shows the XRD analysis results. The TiO_2 (anatase) raw sample shows clear peaks corresponding to the tetragonal anatase phase in Fig. 3(a). The XRD spectra of the planetary-milled samples, however, indicate a high degree of disorder. The milled sample starts showing amorphization in the structure, and the structure gradually converted into the rutile phase materials as the milling time increased. The Ti_9O_{17} phase of a triclinic structure appeared when the powder was reduced at 1,200°C for 3 h [46]. The oxygen content in the TiO_2 raw powder samples was 47.70 wt.% using a C/N/O analyzer, whereas the milled samples contained 34.60 wt.% oxygen. The reduced sample contained only 41.60% oxygen, indicating that milling for 15 h produced more oxygen deficiency than did the reduction process.

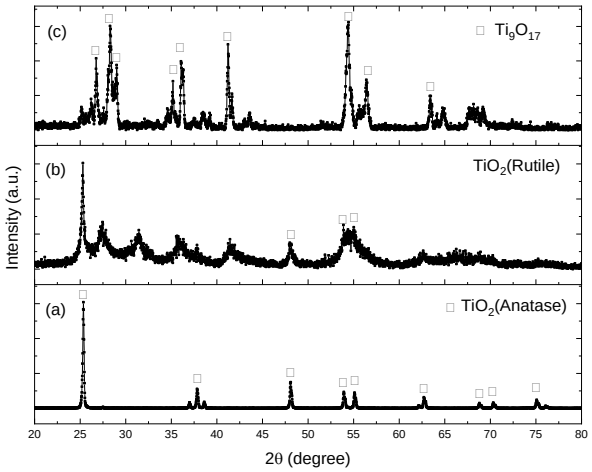

Fig. 3 XRD peaks for various TiO_2 samples. (a) Anatase TiO_2 raw powder, (b) after 15 h planetary milling, and (c) H_2 reduction at 1,200°C for 3 h.

Raman analysis of the samples is shown in Fig. 4. The anataseTiO$_2$ powder (Fig. 4(a)) yielded vibrational energies for the Ti-O bond of 198, 397, 517, and 640 cm^{-1}, which agreed with the values reported previously [47]. The milled sample (Fig. 4(b)) displayed small peaks in addition to the peaks at 435 and 610 cm^{-1}. These peaks were considered to correspond to atomic vibrations resulting from the structure distorted due to oxygen deficiency. The reduced sample (Fig. 4(c)), however, retained a highly crystalline structure with high peak intensities over the range 800 ~ 990 μm.

It is noteworthy that the peak intensities shown in Fig. 4(b) and 4(c) increased significantly over the 800 ~ 990 μm range. In general, the Raman shift transition energy between the rotational levels is <100 cm^{-1} (i.e., >100 μm), while the energy between vibrational levels is 100 ~ 4,000 cm^{-1} (100 ~ 2.50 μm) and the energy between electronic levels exceeds 10,000 cm^{-1} (1 μm) [48]. Thus, the milling and reduction processes enhanced the Ti-O vibrations by loosening individual atoms from the crystal lattice. However, the atomic vibrations alone could not fully explain the emission spectra over the range 3 ~ 20 μm.

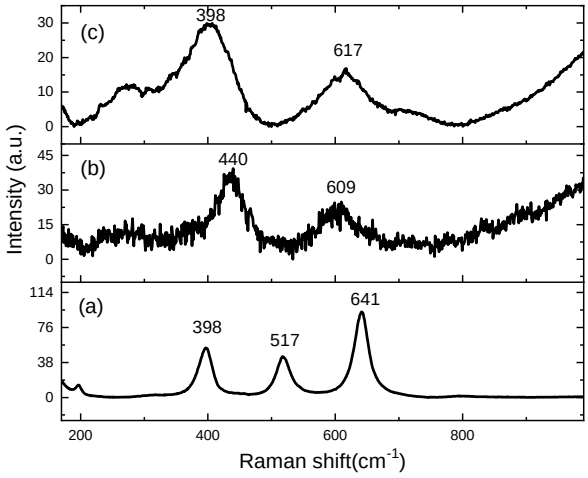

Fig. 4 Raman spectra of various TiO_2 samples. (a) TiO_2 raw powder, (b) with 15 h planetary milling, and (c) with H_2 reduction.

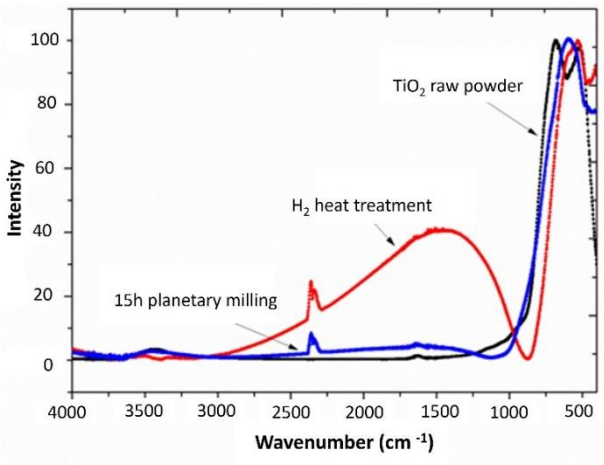

Fig. 5 FT-IR absorbance spectra of the various TiO_2 samples.

The FT-IR absorbance spectra of the samples revealed that the TiO_2 raw powder and the 15 h milled samples showed an increase in absorbance only over the range 500 ~ 1,000 cm^{-1} (10 ~ 20 μm), whereas the reduced samples showed large absorbance peaks over a wider range of 1,000 ~ 3,000 cm^{-1} (3.30 ~ 10 μm). This result, which showed a relative emissivity of 0.902 over the range 3 ~ 7 μm (Fig. 5), was comparable to the high emissivity of the reduced samples and corresponding temperature increase in the aluminum disks coated with lacquer paint.

Calculation of the Energy Levels by DV-Xα Simulation

To relate the phenomena described above to electronic transitions, the DV-Xα method was used to calculate the electronic energy levels of the TiO_2 resulting from each of the different processes. As shown in Fig. 6, (a) $[Ti_9O_{50}]^{-64}$ cluster model was used to model the tetragonal TiO_2 (anatase). The $[Ti_9O_{49}]^{-62}$ cluster model, which contained one vacancy in the middle of the cluster, was employed to simulate the effects of an oxygen vacancy. The $[Ti_9O_{31}]^{-44}$ cluster was employed to model the reduced TiO_2, in accordance with its crystal structure, Ti_9O_{17} (triclinic), as determined by XRD experiments. The clusters used in the calculation included 40 ~ 60 atoms, and the systems were sufficiently large that they were assumed to be accurately predictive. Electronic energy levels were obtained from the DV-Xα simulation. The wavelengths of visible light radiated due to electronic transitions were predicted from the calculated energy levels. Similarly, the wavelengths of FIR may be predicted to some extent according to the energy differences between the upper electronic energy levels and the HOMO (highest occupied molecular orbital) level. Then, the low FIR emissivity of the TiO_2 raw powder over the range 3 ~ 7μm can be ascribed to the presence of a large band gap as shown in Table 3 [6] and Fig. 7. The TiO_2 oxygen defect model for milled powder in Fig. 6(b) predicted a wide range of energy levels, from less than 0.06 – 2.325 eV along with energy gaps of 0.224, 0.276 and 0.609 eV Fig. 7 (b). These results predicted that the powder could potentially radiate at shorter FIR wavelengths of 2.06 ~ 5.62 μm and at long FIR wavelengths of > 20.6 μm, together with a visible emission band at 0.54 μm. However, a low emissivity is predicted due to the presence of band gap of 2.325 eV, and it was observed experimentally. On the other hand, the gaps between the upper levels in the Ti_9O_{17} crystal, i.e., reduced sample in Fig. 6(c), were less than 0.13 eV, such that the upper levels were closely populated with maximum energy gap of 0.221 eV Fig. 7 (c). This crystal was predicted to show characteristics of FIR radiation at long wavelengths, around 9.50 μm, and at short wavelength, 5.59 μm. FIR radiation over the 3 ~ 7 μm range corresponds to 0.17 ~ 0.41 eV energy level differences. The DV-Xα results from the models for milled and reduced TiO_2 powders predict the effective radiation in the 3 ~ 7 μm. Therefore, it can be said that the FIR spectrum over the 3 ~ 7 μm range was attributed, to a certain extent, to electronic excitement caused by absorption of thermal energy available at 250°C in the Ti-O system. The absorption of energy over a range of wavelengths resulted in electron transitions, followed by molecular vibrations within the Ti-O system. Accordingly, unlike the TiO_2 sample containing defects or the Ti_9O_{17} sample, anatase TiO_2 of a wide band gap structure would be expected to yield less FIR radiation in the range of 3 ~ 7 μm.

Table 3 Band gap energies and energy levels of the various TiO_2 samples.

(a) TiO_2 (anatase)			**(c) TiO_2 (vacancy)**			**(c) Ti_9O_{17}**		
E_i	**Energy (eV)**	**ΔE_i**	**E_i**	**Energy (eV)**	**ΔE_i**	**E_i**	**Energy (eV)**	**ΔE_i**
E421 (HOMO)	–2.716	3.332	E415 (HOMO)	–2.652	0.609	E251 (HOMO)	–0.084	0.116
E422 (LUMO)	0.616	0.054	E416	–2.043	2.325	E252 (LUMO)	0.032	0.130
E423	0.670	0.141	E417 (LUMO)	0.282	0.018	E253	0.162	0.074
E424	0.810	0.050	E418	0.300	0.007	E254	0.236	0.022
E425	0.860	0.067	E419	0.307	0.224	E255	0.258	0.117
E426	0.927	0.007	E420	0.531	0.029	E256	0.375	0.025
E427	0.934	0.156	E421	0.560	0.073	E257	0.399	0.081
E428	1.090	0.061	E422	0.633	0.050	E258	0.481	0.065
E429	1.151	0.050	E423	0.684	0.276	E259	0.546	0.058
E430	1.200	0.024	E424	0.960	0.067	E260	0.604	0.014
E431	1.224	0.009	E425	1.027	0.005	E261	0.617	0.221

$\Delta E_i = E_{i+1} - E_i$

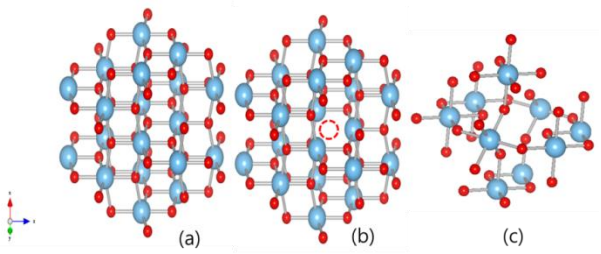

Fig. 6 Cluster models for calculating the electronic energy structures using the DV-Xα molecular orbital method: (a) TiO_2 (anatase) (b) TiO_2 with an oxygen vacancy, a model for the milled powder, and (c) a Ti_9O_{17} cluster model for the product of H_2 reduction.

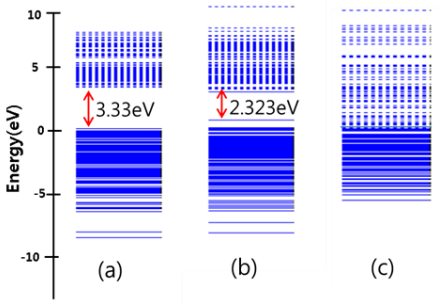

Fig. 7 Electronic energy levels of TiO_2 powders processed differently: (a)TiO_2 (anatase) (b) TiO_2 for oxygen vacancy of milled powder, and (c) Ti_9O_{17} cluster for H_2 reduction.

Conclusion

We have investigated the effects of the defect density on the FIR radiation spectrum in terms of the level of atomic disorder and the oxygen vacancies in the system. Anatase TiO_2 powder was chosen as a model material, and various TiO_2 samples were prepared with reduction or milling process. DV-Xα was used to calculate the electron energy levels to examine the relationship between the electronic transitions and the FIR radiation. The summary and conclusions of the study are as follows:

1. When lacquer paint was heated as a target material, the presence of anatase TiO_2 caused temperature increases of 12.58°C, whereas the milled powder yielded a temperature increase of 17.70°C. On the other hand, the reduced powder resulted in a temperature increase of 24.38°C, indicating that the presence of some vacancies was more effective at increasing the FIR radiation intensity than was a high density of defects in the TiO_2 structure.

2. XRD analysis revealed that the reduced sample changed from TiO_2 to Ti_9O_{17}. This sample displayed a high absorbance peak over the 3 ~ 7 μm range in the FT-IR spectra relative to other samples. This observation was consistent with the high emissivity, 0.932, over the range 3 ~ 20 μm.

TiO_2 with oxygen deficiency, a model for milled powder, yielded a band gap of 2.325 eV with fine gaps among the energy levels of 0.06 ~ 0.22 eV. In particular, Ti_9O_{17}, reduced TiO_2 powder, yielded a narrow energy gap of 0.221 eV, consistent with the temperature increase observed in the lacquer paint. The Ti_9O_{17} sample model and the TiO_2 sample model with an oxygen vacancy gave reasonable predictions of the FIR radiation over the range 3 ~ 7 μm.

Acknowledgements

This work was funded by the Manpower Development Program for Energy & Resources (No. 2008EAPHMP 1300002009), supported by the Ministry of Knowledge and Economy (MKE) of Korea. We gratefully acknowledge the use of facilities at the Research Institute of Advanced Materials, SNU.

References

[1] E. H. Putley, History of infrared detection—part I. The first detectors of thermal radiation, Infrared Phys. 22(3) (1982) 125 – 131.

[2] J. F. Lehmann, D. R. Silverman, B. A. Baum, N. Kirk, V.C. Johnston, Temperature distributions in the human thigh, produced by infrared, hot pack and microwave applications, Arch. Phys. Med. Rehabil. 47(5) (1966) 291 – 299.

[3] Y. Liu, Y. Zeng, X. Hu, X. Sun, Effect of ultrasonic power on water removal kinetics and moisture migration of kiwifruit slices during contact ultrasound intensified heat pump drying, Food Bioproc. Tech. 13 (2020) 430 – 441.

[4] Y. H. Liu, X. F. Li, S. Miao, Y. Yin, W. K. Zhu, Ultrasonic-far-infrared radiation drying characteristics

and microstructure of pumpkin slices, J. Agric. Eng. 32(10) (2016) 10.

[5] Wu, B., Guo, X., Guo, Y., Ma, H., & Zhou, C. Enhancing jackfruit infrared drying by combining ultrasound treatments: Effect on drying characteristics, quality properties and microstructure, Food Chem. 358 (2021) 129845.

[6] X. Shi, Y. Yang, Z. Li, X. Wang, Y. Liu, Moisture transfer and microstructure change of banana slices during contact ultrasound strengthened far-infrared radiation drying, Innov. Food Sci. Emerg. Technol. 66 (2020) 102537.

[7] H. P. Baltes, F. K. Kneubühl, Spectral distribution of cavity black body radiation in the far infrared, Phys. Lett. A. 30(6) (1969) 360 – 362.

[8] E. M. Sparrow, Radiation heat transfer, Routledge, 27 April 2018, (2018).

[9] A. Leupin, H. Vetsch, F. K. Kneubuehl, Investigation, comparison and improvement of technical infrared radiators. Infrared physics, 30(3) (1990) 199 – 258.

[10] Y. M. Ke, M. C. Ou, C. K. Ho, Y. S. Lin, H. Y. Liu, W. A. Chang, Effects of somatothermal far-infrared ray on primary dysmenorrhea: a pilot study, J. Evid. Based Complementary Altern. Med. (1) (2012) 240314.

[11] T. M. Silva, G. A. Moreira, A. A. J. Quadros, M. Pradella-Hallinan, S. Tufik, A. S. B. Oliveira, Effects of the use of MIG3 bioceramics fabrics use-long infrared emitter-in pain, intolerance to cold and periodic limb movements in post-polio syndrome, Arq. Neuropsiquiatr. 67 (2009) 1049 – 1053.

[12] T. K. Leung, C. H. Kuo, C. M. Lee, N. W. Kan, C. W. Hou, Physiological effects of bioceramic material: harvard step, resting metabolic rate and treadmill running assessments, Chin. J. Physiol. 56(6) (2013) 334 – 40.

[13] R. F. Nunes, F. J. Cidral-Filho, L. J. Flores, F. Y. Nakamura, H. F. Rodriguez, F. Bobinski, L. G. Guglielmo, Effects of far-infrared emitting ceramic materials on recovery during 2-week preseason of elite futsal players, J. Strength Cond. Res. 34(1) (2020) 235 – 248.

[14] L. Zhang, P. Chan, Z. M. Liu, L. L. Hwang, K. C. Lin, W. P. Chan, C. S. Choy, The effect of photoluminescence of bioceramic irradiation on middle cerebral arterial occlusion in rats, J. Evid. Based Complementary Altern. Med. (1) (2016) 7230962.

[15] T. K. Leung, Y. S. Lin, Y. C. Chen, H. F. Shang, Y. H. Lee, C. H. Su, T. M. Chang, Immunomodulatory effects of far-infrared ray irradiation via increasing calmodulin and nitric oxide production in raw 264.7 macrophages, Biomed. Eng. - Appl. Basis Commun. 21(05) (2009) 317 – 323.

[16] D. Lee, Y. W. Kim, J. H. Kim, M. Yang, H. Bae, I. Lim, J. H. Ko, Improvement characteristics of bio-active materials coated fabric on rat muscular mitochondria, Korean J. Physiol. Pharmacol., KJPP. 19(3) (2015) 283.

[17] R. F. Rosas, A. A. Emer, A. P. Batisti, D. D. Ludtke, B. L. Turnes, F. Bobinski, D. F. Martins, Far infrared-emitting ceramics decrease Freund's adjuvant-induced inflammatory hyperalgesia in mice through cytokine modulation and activation of peripheral inhibitory neuroreceptors, J. Integr. Med. 16(6) (2018) 396 – 403.

[18] Y. Chang, The effect of far infrared radiation therapy on inflammation regulation in lipopolysaccharide-induced peritonitis in mice, SAGE Open Med. 6 (2018) 2050312118798941.

[19] S. Fujita, Y. Ikeda, M. Miyata, T. Shinsato, T. Kubozono, S. Kuwahata, C. Tei, Effect of Waon therapy on oxidative stress in chronic heart failure, Circ. 75(2) (2011) 348 – 356.

[20] T. K. Leung, Y. S. Lin, C. M. Lee, Y. C. Chen, H. F. Shang, S. Y. Hsiao, J. S. Chao, Direct and indirect effects of ceramic far infrared radiation on the hydrogen peroxide-scavenging capacity and on murine macrophages under oxidative stress, J. Med. Biol. Eng. 31(5) (2011) 345 – 51.

[21] K. Yamashita, The effects of the far-infrared ray (FIR) energy radiation on living body, Blood Cell-An Overview of Studies in Hematology (2012) 21 September 2012.

[22] L. Peng, B. Su, A. Yu, X. Jiang, Review of clothing for thermal management with advanced materials, Cellulose. 26 (2019) 6415 – 6448.

[23] A. Martínez Nova, F. Marcos-Tejedor, B. Gómez Martín, R. Sánchez-Rodríguez, E. Escamilla-Martínez, Bioceramic-fiber socks have more benefits than cotton-made socks in controlling bacterial load and the increase of sweat in runners, Text. Res. J. 88(6) (2018) 696 – 703.

[24] T. Harifi, M. Montazer, Application of nanotechnology in sports clothing and flooring for enhanced sport activities, performance, efficiency and comfort: a review, J. Ind. Text. 46(5) (2017) 1147 – 1169.

[25] P. H. Hoet, I. Brüske-Hohlfeld, O. V. Salata, Nanoparticles–known and unknown health risks, J. Nanobiotechnology. 2 (2004) 1 – 15.

[26] G. P. Dransfield, Inorganic sunscreens, Radiat. Prot. Dosimetry. 91(1-3) (2000) 271 – 273.

[27] S. L. Schneider, H. W. Lim, A review of inorganic UV filters zinc oxide and titanium dioxide, Photodermatol. Photoimmunol. Photomed. 35(6) (2019) 442 – 446.

[28] C. Cole, T. Shyr, H. Ou-Yang, Metal oxide sunscreens protect skin by absorption, not by reflection or scattering. Photodermatology, Photodermatol. Photoimmunol. Photomed. 32(1) (2016) 5 – 10.

[29] K. Vos, H. J. Krusemeyer, Reflectance and electroreflectance of TiO_2 single crystals. I. Optical spectra, J. Phys. C: Solid State Phys.10(19) (1977) 3893.

[30] J. F. Muth, R. M. Kolbas, A. K. Sharma, Oktyabrsky, S., & Narayan, J. Excitonic structure and absorption coefficient measurements of ZnO single crystal epitaxial films deposited by pulsed laser deposition, J. Appl. Phys. 85(11) (1999) 7884 – 7887.

[31] T. G. Smijs, S. Pavel, Titanium dioxide and zinc oxide nanoparticles in sunscreens: focus on their safety and effectiveness, Nanotechnol. Sci. Appl. (2011) 95 – 112.

[32] T. Hoang-Minh, T. L. Le, J. Kasbohm, R. Gieré, UV-protection characteristics of some clays, Appl. Clay Sci. 48(3) (2010) 349 – 357.

[33] E. F. Bernstein, H. W. Sarkas, P. Boland, Iron oxides in novel skin care formulations attenuate blue light for enhanced protection against skin damage, J. Cosmet. Dermatol. 20(2) (2021) 532 – 537.

[34] H. Yin, P. S. Casey, M. J. McCall, Surface modifications of ZnO nanoparticles and their cytotoxicity, J. Nanosci. Nanotechnol. 10(11) (2010) 7565 – 7570.

[35] P. Porrawatkul, P. Nuengmatcha, A. Kuyyogsuy, R. Pimsen, P. Rattanaburi, Effect of Na and Al doping on ZnO nanoparticles for potential application in

sunscreens, J. Photochem. Photobiol. B. 40 (2023) 112668.

[36] C. Kormann, D. W. Bahnemann, M. R. Hoffmann, Environmental photochemistry: Is iron oxide (hematite) an active photocatalyst? A comparative study: α-Fe2O3, ZnO, TiO2, J. Photochem. Photobiol. A Chem. 48(1) (1989) 161 – 169.

[37] S. Lee, Y. Kim, S. Kang, Far-infrared emission of Ti-based oxides, J. Mol. Struct. 987(1-3) (2011) 86 – 90.

[38] H. Adachi, M. Tsukuda, C. Satoko, Discrete variational Xα cluster calculations. I. Application to metal clusters, J. Phys. Soc. Jpn. 45(3) (1978) 875 – 883.

[39] M. Tsukada, C. Satoko, H. Adachi, Theory of the Surface Electronic Structure and Defect States of Rutile by the DV–Xα Cluster Calculation, J. Phys. Soc. Jpn. 47(5) (1979) 1610 – 1619.

[40] J. C. Slater, A simplification of the Hartree-Fock method. Physical review, 81(3) (1951) 385.

[41] D. E. Ellis, H. Adachi, F. W. Averill, Molecular cluster theory for chemisorption of first row atoms on nickel (100) surfaces, Surf. Sci. 58(2) (1976) 497 – 510.

[42] J. K. Wilmshurst, Vibrational spectra of inorganic molecules: Part I. antimony pentachloride, antimony trichloride, zirconium tetrachloride, and ferric chloride, J. Mol. Spectrosc. 5(1-6) (1961) 343 – 354.

[43] N. Hosaka, T. Sekiya, C. Satoko, S. Kurita, Optical properties of single-crystal anatase TiO_2, J. Phys. Soc. Jpn. 66(3) (1997) 877-880.

[44] H. Nakamatsu, H. Adachi, S. Ikeda, Electronic structure of the valence band for perovskite-type titanium double oxides studied by XPS and DV-Xα cluster calculations, J. Electron Spectros. Relat. Phenomena. 24(2) (1981) 149 – 159.

[45] I. Nakagawa, S. I. Mizushima, A. J. Saraceno, T. J. Lane, J. V. Quagliano, Infrared absorption spectra of inorganic co-ordination complexes—XV: Normal vibrations of sulfamic acid, H_3N^+—SO_3^-, Spectrochim. Acta. 12(2-3) (1958) 239 – 243.

[46] P. Strobel, Y. Le Page, Growth of Ti/sub9/O/sub 17/crystals by chemical vapor transport. J. Cryst. Growth;(Netherlands). 56(3) (1982).

[47] T. Ohsaka, F. Izumi, Y. Fujiki, Raman spectrum of anatase, TiO2, J. Raman Spectrosc. 7(6) (1978) 321 – 324.

[48] R. J. Butcher, W. J. Jones, Cyclopropane: Studies of some vibration-rotation Raman bands, J. Mol. Spectrosc. 47(1) (1973) 64 – 83.